A systematic study of the synthesis of transition metal phosphides and their activity for hydrodeoxygenation of phenol

C. V. M. Inocencio, Priscilla Magalhaes de Souza, R. C. Rabelo-Neto, V. T. da Silva, Fabio Bellot Noronha

A systematic study of the synthesis of transition metal phosphides and their activity for hydrodeoxygenation of phenol

Carlos V. M. Inocêncio[1,2], Priscilla Magalhães de Souza[1,3], Raimundo Crisostomo Rabelo-Neto[2], Victor Teixeira da Silva[1], Fabio Bellot Noronha[2,3,4]*

[1] Federal University of Rio de Janeiro, Chemical Engineering Program – COPPE, 21941-972, Rio de Janeiro, RJ, Brazil.

[2] Catalysis Division, National Institute of Technology, Av. Venezuela 82, 20081-312, Rio de Janeiro, RJ, Brazil.

[3] Univ. Lille, CNRS, Centrale Lille, ENSCL, Univ. Artois, UMR 8181 – UCCS – Unité de Catalyse et Chimie du Solide, F-59000 Lille, France

[4] Military Institute of Engineering, Chemical Engineering Department, Praça Gal. Tiburcio 80, Rio de Janeiro, 22290-270, Brazil.

Corresponding author: fabio.bellot@int.gov.br

Submitted to

Catalysis Today

Revised July 2020

Abstract

Five different unsupported transition metal phosphides were synthesized and tested for hydrodeoxygenation of phenol in gas phase at 300 ° C and atmospheric pressure. The metal phosphide phases were synthesized in two steps: synthesis of phosphates and temperature programmed reduction. *In situ* X-ray diffraction and temperature programmed reduction revealed the formation of the phosphide phases: Ni_2P, MoP, CoP/CoP_2, FeP and WP. The *in situ* diffractograms showed that the metal phosphate precursor is decomposed during reduction, producing metal oxide (Molybdenum) or pyrophosphate (Nickel, Iron) phases, without the formation of a metallic phase. All catalysts showed high selectivity to direct deoxygenation products, indicating that the phosphide phases promoted the direct cleavage of C-O bond. However, product distribution varied significantly depending on the metal phosphide phase. Ni_2P catalyst exhibited the highest selectivity to benzene, whereas CoP, FeP and WP showed a significant formation of cyclohexene. FeP also produced cyclohexane, while a large amount of $C_5 – C_6$ hydrocarbons was formed over MoP. Product distribution was correlated to the type of crystal structure of transition metal phosphides.

Keywords: Hydrodeoxygenation; Phenol; Transition metal phosphide; Characterization of metal phosphides.

1. Introduction

The lignocellulosic biomass can be used as a renewable feedstock for the production of chemical products and fuels [1,2]. Different technologies are proposed for the conversion of lignocellulosic biomass such as fast pyrolysis that produces the so-called bio-oil [3]. Although the bio-oil presents very low contents of sulfur and nitrogen [4], which is highly desired, it contains a high percentage of oxygenated compounds in comparison to fossil fuels. As a result, bio-oil has several undesired properties such as high corrosivity, low energy density and high thermal and chemical instability, which inhibits its direct utilization as a fuel for vehicles and, therefore, it has to be upgraded. The hydrodeoxygenation process (HDO) is a potential technology for the bio-oil upgrading that uses hydrogen to remove oxygen in the presence of a catalyst. One of the challenges of this technology is the development of a catalyst that is active, selective and stable under reaction conditions. Due to the complex composition of the bio-oil, model molecules such as phenol, anisole, guaiacol have been used on the studies about catalysts for HDO reaction. Different catalysts have been investigated for HDO of model compounds such as transition metals and noble metals [5-14]. These studies demonstrated that the type of the metal [13,14] and support [5,6,8] strongly affects the deoxygenation activity. Oxophilic metals and supports such as Ru and niobia, respectively, favor the selectivity to deoxygenated products, which was attributed to the strong adsorption of the oxygen from the model molecule to the metal or support.

Recently, phosphide catalysts have been successfully used for the HDO of different model molecules [15-24]. In comparison to noble metal catalysts, they are less expensive and exhibits higher activity to deoxygenation. For instance, Ni phosphide phase exhibited higher deoxygenation activity than the metallic Ni phase for the HDO of m-cresol over Ni_2P/ZrO_2, Ni_2P/SiO_2, Ni/ZrO_2 and Ni/SiO_2 [15]. In addition, the nature of Ni phosphide

phase plays a role on the HDO reaction. De Souza et al. [25] reported that Ni_2P phase favors the selectivity to benzene, whereas $Ni_{12}P_5$ phase led to the formation of hydrogenation products.

The type of transition metal phosphide also affects the activity and selectivity to deoxygenation products. Whiffen and Smith [22] reported a higher activity of Ni_2P compared to MoP (both unsupported) for the HDO of 4-methylphenol at 350 ºC and 4.4 MPa. While Ni_2P presented a higher selectivity to direct deoxygenation (DDO) route than hydrogenation (HYD) route, the selectivity to both reaction pathways was similar in the presence of MoP. Rodríguez-Aguado et al. [23] evaluated the performance of silica supported Ni_2P and FeP for the HDO of phenol at 300 ºC and 1.5 MPa. For the FeP catalyst, the major products detected were cyclohexene (64.5 %) and cyclohexane (35.5 %). When the reaction was carried out over Ni_2P, cyclohexane (70.2 %) and cyclohexanol (24.7 %) were formed, with small amounts of cyclohexene and benzene. Berenguer et al. [24] compared the activity of Ni_2P and Co_2P supported on hierarchical zeolites for the HDO of phenol at 220 ºC and 4 MPa. Cyclohexane was the main product over Ni_2P/h-ZSM-5 and Ni_2P/h-Beta catalsysts, representing about 95 % and 85 % of selectivity, respectively. In addition, a mixture of compounds containing two C_6-rings (10 %) was also formed in the presence of Ni_2P/h-Beta. Cyclohexane was also the main product over Co_2P/h-ZSM-5 and Co_2P/h-Beta catalysts (around 60 %). However, cyclopentane was obtained over Co_2P/h-ZSM-5, whereas the two C_6-rings mixture was significantly formed over Co_2P/h-Beta. He and Laursen [26] performed a DFT study for HDO of phenol using 1st row transition metal phosphide catalysts (TiP, VP, CrP, Fe_2P, Co_2P and Ni_2P) at 300 ºC and 1 atm. According to the authors, these phosphides exhibit enhanced activity towards oxygen, which favors C-O cleavage. In contrast, they present limited hydrogenation activity, which avoids overhydrogenation.

Although few works performed a systematic study comparing the performance of different transition metal phosphides for HDO of guaiacol [17] or 2-methyltetrahydrofuran [27], there are no study for HDO of phenol reaction using a wide range of metal phosphides.

Therefore, the aim of this work was to investigate the effect of the type of transition metal phosphide on the HDO of phenol reaction in gas phase at 300 ºC and 1 atm . Different unsupported metal phosphides (nickel, cobalt, iron, molybdenum and tungsten) were prepared and characterized by *in situ* X-ray diffraction to identify the phases formed, and tested for the HDO of phenol. A correlation between phosphide structure and direct deoxygenation activity was proposed.

2. Experimental

2.1. Catalyst preparation

The unsupported metal phosphides were prepared by temperature programmed reduction (TPR) method [28] and involved the formation of phosphate precursor and its reduction to phosphide.

In the first step, the metal precursor ($Ni(NO_3)_2{\cdot}6H_2O$, $Co(NO_3)_2{\cdot}6H_2O$, $Fe(NO_3)_3{\cdot}9H_2O$, $(NH_4)_6Mo_7O_{24}{\cdot}4H_2O$) and ammonium hydrogen phosphate ($(NH_4)_2HPO_4$) were solubilized, separately, in water, except for tungstic acid (H_2WO_4) that had to be solubilized in aqueous ammonia. Then, the solution of $(NH_4)_2HPO_4$ was slowly dripped into the metal precursor solution under constant stirring. Then, for nickel and cobalt phosphide synthesis, nitric acid was added to the mixture until complete solubilization of the precipitate. This step was unnecessary for the other metals. The obtained solution was placed in a silicone bath held at 105 ° C under stirring. Then, a gel was formed, which was dried at 150 °C. The solid was calcined at 500 °C for 6 h (10 °C min^{-1}). Before catalytic tests, this material was reduced *ex situ* using two heating steps with different rates: 30 ºC to T_1 (10 °C min^{-1}), T_1 to T_2 (1 °C min^{-1}), in which T_1 and T_2 represents the intermediate and final activation temperatures, respectively. These values aforementioned were selected according to TPR profiles and are presented on (Table 1). Hydrogen was fed into the reactor with a flow rate of 1 mL min^{-1} per 1 mg of phosphate precursor. Then, the reactor was cooled to room temperature and fed with a 30 mL min^{-1} of 0.5 % O_2/N_2 mixture for, approximately, 16 h. The unsupported metal phosphides precursors were prepared with the following P/Metal molar ratio: $Ni_xP_yO_z$ (0.8); $Co_xP_yO_z$ (1.5); $Fe_xP_yO_z$ (1.0); $Mo_xP_yO_z$ (1.0); $W_xP_yO_z$ (1.0).

2.2. Catalyst characterization

In situ XRD was carried out for unsupported nickel, cobalt, iron and molybdenum phosphide catalysts at XRD1 beamline of the Brazilian Synchrotron Light Laboratory (LNLS) [29]. The sample (20 – 30 mg) was placed in a quartz capillary of 1 mm internal diameter between two pieces of quartz wool. The capillary was added to a reaction cell connected to diffractometer of 3 circles of Newport (model N3050-P1). Diffratograms were measured in the 2θ range of 5 to 100° using an array of 24 Mythen detectors (DECTRIS). The temperature of analysis was controlled with a robotic arm (Yaskawa) used to maintain a blower (FMB Oxford (GSB1300 model) of hot air above the capillary. A Si double crystal monochromator (111) positioned more than 10 m before the experimental station selected the wavelength equal to 1.0332 Å. The instrument was calibrated using an Al_2O_3 standard (SRM 640a / NIST). The measurements were performed with a flow rate of 10 mL min^{-1} of pure H_2 in the capillary and with two heating ramps. Initially, the samples were warmed from room temperature to 400 °C at 10 °C min^{-1}. Then, the samples were heated at 3 °C min^{-1} from 400 ºC up to the final synthesis temperature: 650 ºC for Ni_2P, CoP e MoP, and 700 ºC for FeP. To facilitate the identification of each phase, the Bragg angles obtained in XRD1 line were converted to the ones using a copper tube source.

The XRD patterns of WP were obtained using a Rigaku-Miniflex powder diffractometer with a copper tube (λ = 1.5418 Å) and operated at 30 kV and 15 mA. The diffraction data were obtained in 0.05° steps in the range $10 < 2\theta < 90°$ and scanning speed of 2^o min^{-1}. Before analysis, WP was obtained by ex-situ reduction of its precursor and passivation following the same procedure previously described.

Temperature programmed reduction (TPR) was performed in a multipurpose system coupled to a Pfeiffer Vacuum mass spectrometer (MS) model QME 200. Prior to reduction,

the samples (0.1 g) were pretreated under He (50 mL/min) at 450 °C (10 °C/min) for 30 min and then cooled to 30 °C. The samples were reduced under pure H_2 (100 mL/min H_2) at a heating rate of 1 °C/min up to 1000 °C.

The CO chemisorption analyses were carried out to measure the number of active sites on the surface of the catalysts using pulses of CO. Before the CO adsorption, the samples were treated under the same conditions described for TPR experiments, except for the final temperature which has been applied T_2 instead of 1000 ºC, and then, it was purged under He. After cooling to room temperature, pulses of a mixture containing 5% CO in He were injected in the reactor and the gases were monitored by a Pfeiffer Vacuum mass spectrometer (MS) model QME 200.

2.3. Catalytic experiments

The hydrodeoxygenation of phenol was carried out in a gas phase fixed bed quartz reactor, operating at atmospheric pressure and 300 ºC. Prior to the reaction, the sample was reduced *ex situ* as mentioned previously. The amount of catalyst used for HDO of phenol reaction is reported in Table 3. The reactivation was performed under pure hydrogen (30 mL min^{-1}) at 300 ºC (for nickel, cobalt and molybdenum) or 500 ºC (for iron and tungsten) for 1h (10 ºC/min). The reaction mixture was obtained by flowing H_2 (at the same flow rate used in reactivation) through a saturator containing phenol, which was kept at the specific temperature required to obtain the desired H_2/phenol molar ratio (about 60). To avoid condensation, all lines were heated to 220 ºC. The reaction products were analyzed by a gas chromatograph (GCMS Agilent Technologies – Model 7890 A), using Innowax capillary column and a flame-ionization detector (FID).

The phenol conversion, selectivity for each product and reaction rate were calculated as follows:

$$Conversion\ (\%) = \frac{\left(mol_{phenol}^{fed} - mol_{phenol}^{out}\right)}{mol_{phenol}^{fed}}\ x\ 100 \qquad 8$$

(1)

$$Selectivity\ (\%) = \frac{mol\ of\ product\ produced}{mol\ of\ phenol\ consumed} \times 100 \quad (2)$$

$$Reaction\ rate\ \left(\frac{\mu mol}{min \cdot g}\right) = \frac{\left((molar\ flow)_{phenol}^{fed} \times conversion_{phenol}\right)}{catalyst\ mass} \quad (3)$$

Turnover frequency of catalysts were calculated taking into account the number of active sites by two methods: through the values of CO chemisorption and by the crystallite diameter obtained from XRD analyses. For the last one, crystallite diameter was calculated from Scherrer equation and it was considered that the dispersion of catalyst corresponds to the inverse of crystallite diameter, in nanometer [30].

3. Results and discussion

3.1 Catalyst characterization

The phase transitions of unsupported metal phosphide catalysts observed during phosphate reduction were investigated by *in situ* XRD for $Ni_xP_yO_z$; $Mo_xP_yO_z$; $Co_xP_yO_z$; and $Fe_xP_yO_z$. Fig. 1 shows the diffractograms obtained during reduction of $Ni_xP_yO_z$. No lines are detected on the diffractogram of the calcined sample, indicating the presence of an amorphous phase. The diffraction lines characteristic of $Ni_{12}P_5$ (JCPDS 22-1190) and Ni_2P (JCPDS 03-0953) phases appears at 510 ºC. Increasing the temperature to 533 ºC reduced significantly the intensities of the lines attributed to $Ni_{12}P_5$ phase, which are no longer observed at 570 ºC. On the other hand, the intensities of the lines of the Ni_2P phase continuously increased, which indicates that the $Ni_{12}P_5$ is transformed into Ni_2P phase. After 616 °C, the diffractogram exhibits the lines characteristic of the Ni_5P_4 phase but they are no longer observed after heating at 650 °C. At this reduction temperature, only the lines typical of the Ni_2P phase are observed.

The crystalline phases transformations during the reduction of oxidic precursors ($NH_4NiPO_4{\cdot}nH_2O$) for the preparation of bulk Ni_2P with a P/Ni ratio of 0.8 (the same ratio used in this work) were investigated by Rodriguez et al. [31] using synchrotron-based time-resolved X-ray diffraction. The diffractograms of the fresh sample exhibit the lines corresponding to $NH_4NiPO_4 \cdot nH_2O$ phase. The intensities of these lines continuously decreased when the sample was heated from 25 to 400 ºC. Mass spectrometer revealed the evolution of water and ammonia into the gas phase. After 400 ºC, all of the diffraction lines disappear and the sample becomes amorphous. According to the authors, the removal of water and ammonia causes the collapse of the structure, which explain why the sample is amorphous. This result agrees very well with the absence of diffraction lines on the diffractogram of our sample that was previously calcined at 500 ºC. This temperature was

sufficiently high to remove water and ammonia, producing an amorphous sample. From 400 to 650 ^{o}C, no diffraction lines were detected. The Ni_2P phase was formed in the temperature range of 650 to 800 ^{o}C. No lines corresponding to $Ni_{12}P_5$ phase was observed, which is likely due to the different reduction conditions used in both works. In our work, the sample was reduced under pure H_2 at two different heating rates (10 °C min^{-1} from room temperature to 400 ºC and 3 °C min^{-1} from 400 ºC up to 650 ºC), whereas a gas mixture of 5% H_2/95% He and a heating rate of 15 ^{o}C/min was used by Rodriguez et al [31]. The lower heating rate used in our work probably allowed to monitor the formation of the $Ni_{12}P_5$ phase. Berhault et al. [32] used *in situ* X-ray diffraction, *in situ* X-ray absorption spectroscopy (XAS) and magnetic susceptibility techniques to study the reduction of the ammonium nickel phosphate $NiNH_4PO_4 \cdot H_2O$ precursor for the synthesis of bulk Ni_2P with a P/Ni ratio of 7.0. The *in situ* diffractograms showed the lines characteristic of $NiNH_4PO_4 \cdot H_2O$ between room temperature to 250°C. No lines were detected when the sample was heated from 300 to 500 °C, indicating the formation of an amorphous phase. *In situ* XAS study and magnetic susceptibility measurements showed that the nickel pyrophosphate phase ($Ni_2P_2O_7$) corresponds to the amorphous phase on the diffractograms. Furthermore, Liu et al. [33] demonstrated by Raman spectroscopy visible/ UV spectroscopy that the calcined precursor contains a mixture of $Ni_2P_2O_7$ and $Ni_3(PO_4)_2$ phases. In our work, the precursor was calcined at 500 °C, which explain the presence of an amorphous phase on the diffractogram of the calcined sample that it is likely due to $Ni_2P_2O_7$ and $Ni_3(PO_4)_2$ phases. Berhault et al. [32] also observed the appearance of the lines characteristic of Ni_2P phase on the diffractograms of the sample heated above 500 °C, but the $Ni_{12}P_5$ phase was not detected. It is likely that the excess of $(NH_4)_2HPO_4$ used in the synthesis favored the transition from $Ni_{12}P_5$ to Ni_2P and, as result, it may become harder to detect the $Ni_{12}P_5$ phase on the diffractogram. Even in our work, the temperature range in which the $Ni_{12}P_5$ phase

was observed is very narrow ($\Delta T = 60^{o}C$). Considering that in the experiment performed by Berhault et al. [32], the diffractograms were recorded at every 50 ºC heating, it is likely that $Ni_{12}P_5$ phase was formed but it was not detected. However, it is important to stress that the P/Ni ratio may also affect the type of phosphide phase formed [19,34]. For the catalysts containing a low P/Ni ratio, the $Ni_{12}P_5$ is the main phase whereas increasing the P/Ni ratio the Ni_2P phase is preferentially formed. Finaly, the Ni_5P_4 phase detected in our work was not observed by Rodriguez et al. [31] and Berhault et al. [32]. In our work, the excess of phosphorous used in the preparation of the unsupported nickel phosphide catalyst might be incorporated into the lattice of the Ni_2P phase, producing Ni_5P_4 phase at high temperature. In fact, the Ni-P phase diagram reveals the presence of both Ni_2P and Ni_5P_4 phases when atomic percentage of P is between 33.8-44.5 % [35]. Further increase in the temperature led to the disappearance of Ni_5P_4 phase, which is likely due to the removal of phosphorus through the evolution of PH_3 that it has been reported in the literature [36]. Therefore, the decrease in the concentration of phosphorus led to the transformation of Ni_5P_4 to Ni_2P phase, as shown in the Ni-P diagram [35]. The different experimental conditions used by Rodriguez et al. [31] and Berhault et al. [32] could prevent the formation and detection of this phase.

The diffractograms obtained during the reduction of the $Mo_xP_yO_z$ sample are shown in Fig. 2. The diffractogram of the calcined sample exhibits the lines attributed to the $Mo(OH)_3PO_4$ phase (PDF#11-0333), which were also observed by Rodriguez et al. [31] for bulk MoP. There is also a sharp peak at around 28^{o} that is due to the scattering of the beam caused by the capillary holder [29]. The lines attributed to $Mo(OH)_3PO_4$ phase completely disappeared after heating at 233 ºC and new lines corresponding to MoO_3 (PDF#35-0609) and $MoOPO_4$ as well as a broad peak related to an amporphous structure were observed, in agreement with the results reported by Lister et al. [37]. Taking into account that Lister et al. [37] synthesized the $Mo(OH)_3PO_4$ phase using $MoO_3 + H_3PO_4$, and the decomposition of

$Mo(OH)_3PO_4$ phase produced $MoOPO_4$, the phase transformations observed in our diffractograms could be attributed to the reactions described in eqs. 4 and 5. The intensity of these lines decreased and completely disappeared at 412 ºC. The lines characteristic of MoP phase are only detected at 518 ºC. These result suggests that MoP is likely produced by the reduction of $MoOPO_4$ according to eq. 6. Increasing the temperature up to 648 ºC increased the intensity of the lines of MoP phase, indicating that sintering occurs.

$$Mo(OH)_3PO_4 \rightarrow MoO_3 + H_3PO_4 \quad (4)$$

$$MoO_3 + H_3PO_4 + ½\ H_2 \rightarrow MoOPO_4 + 2\ H_2O \quad (5)$$

$$MoOPO_4 + 5\ H_2 \rightarrow MoP + 5\ H_2O \quad (6)$$

Rodriguez et al. [31] studied the synthesis of bulk MoP phase with the same P/Mo ratio employed in this work (P/Mo = 1.0), using time-resolved XRD experiments. The phosphate precursor ($Mo(OH)_3PO_4$) was heated under a gas mixture of 5%H_2 in He at a heating rate of 15 ºC/min. After heating the sample at 350 ºC, the lines characteristic of $Mo(OH)_3PO_4$ were no longer detected, while weak diffraction lines of MoO_3 and a broad peak corresponding to amorphous material are observed. The diffraction lines of MoO_2 phase appears between 600 – 700 ºC and the MoP phase is formed at 800 ºC. The different experimental conditions (hydrogen content of reducing gas and heating rate) used in our work in comparison to the work of Rodriguez et al. [31] could be responsible for the differences in phase transformation observed.

Clark and Oyama [38] investigated the evolution of different phases during reduction of $MoPO_x/Al_2O_3$ sample by *ex situ* XRD of the quenched sample after heating at different temperatures. The diffractogram of the calcined sample revealed the lines of MoO_3, which was reduced to MoO_2 at 490 ºC. Metallic Mo was detected at 600 ºC and MoP phase was

only formed at high temperature (900 ºC). According to Clark and Oyama [38], the presence of MoO_3 instead of the precursor phosphate on the calcined sample was due to the removal of phosphate by alumina. This might also explain the differences in phase transformation observed between our work and Clark and Oyama's work.

Fig. 3 shows the XRD patterns during reduction of the $Co_xP_yO_z$ sample. The diffractogram of the sample after reduction at 174 ºC shows the main line corresponding to $Co(PO_3)_2$ (PDF#27-1120). Increasing the temperature to 518 ºC caused the crystallization of this phase. The lines attributed to CoP phase (PDF#65-2593) are only detected at 645 ºC. However, it is also noticed the presence of lines characteristic to CoP_2 phase (PDF#77-263), indicating that a mixture of these two cobalt phosphide phases are produced at the final reduction temperature.

Wang et al. [40] studied the effect of Co/P ratio on the type of cobalt phosphide phase. The diffractograms of the reduced and passivated samples revealed the formation of Co_2P for the samples with Co/P ratios of 3/1, 2/1 and 3/2, while the CoP phase was observed for the catalyst containing a Co/P ratio of 1/1. In our work, the presence of CoP_2 phase could be attributed to the excess of phosphorous used in the synthesis of the phosphate sample.

The diffractograms of $Fe_xP_yO_z$ sample at different reduction temperatures are shown in Fig. 4. The diffractogram of the calcined sample exhibits the lines corresponding to the quartz type and tridymite type iron phosphate ($FePO_4$) [39]. The diffractograms remained unchanged as the reduction temperature increased up to 412 ºC. Further increase in the temperature to 548 ºC led to the disappearance of the lines attributed to $FePO_4$, and a new phase is formed that corresponds to the iron pyrophosphate phase ($Fe_2P_2O_7$) [39]. At 700 ºC, $Fe_2P_2O_7$ is reduced producing the FeP phase (ICSD Coll. Code 15057).

Wang et al. [40] prepared bulk iron phosphides with various Fe/P ratios (0.5; 1.0; 2.0; 3.0) by the TPR method. After reduction at 647 ºC followed by passivation, the

diffractograms of the catalysts exhibited different phases depending on the Fe/P ratio: FeP (0.5); Fe_2P (1.0; 2.0) and Fe_3P (3.0). In our work, the Fe_2P phase was not detected during the *in situ* reduction of $Fe_xP_yO_z$ as observed by Wang et al. [40] for a sample with the Fe/P = 1.0. According to them, the deficiency in phosphorous on the phosphide formed after TPR was caused by the evolution of phosphorus as PH_3 during the reduction. In our work, the expected FeP was produced, indicating that the loss of phosphorous was not significant in our experiment for this catalyst.

For the $W_xP_yO_z$ sample, the XRD pattern of the calcined sample (not shown) did not exhibit any peak, indicating the presence of an amorphous material. The diffractogram of the sample after reduction at 750 ^oC is shown in Fig. 5. The XRD pattern corresponds to the formation of WP phase (PDF#29-1364).

Clark et al. [41] studied the synthesis of tungsten phosphide by quenching the samples at various reduction temperatures and performing XRD analysis. The diffractogram of tungsten phosphate was amorphous, which agrees very well with our result. WP phase was formed after reduction at 580 ^oC and no other phase was detected at increasing reduction temperatures (600, 620, 665 and 700^oC).

The results obtained through the *in situ* XRD experiments shed light on the synthesis mechanism of the different bulk metal phosphides, by accompaning all the phase transformations that occurred during the reduction. Therefore, the diffractograms of all samples after activation at 650 ºC, 700 ºC and 750 ºC (depending on the metal phosphide) demonstrated that the phosphide phases are formed for all transition metals: Ni_2P, CoP/CoP_2, FeP, MoP, WP. They also revealed that the metal phosphate precursor is decomposed during reduction, producing new phosphate (molybdenum) or pyrophosphate (nickel, iron) phases, which are reduced, producing the phosphide phase without the formation of a metallic phase.

The crystallite size of the phosphide phases were calculated from the diffractograms presented in Figs. 1 – 5 after reduction of the samples at 650 ºC (for Ni_2P, CoP and MoP), 700 ºC (for FeP) and 750 ºC (for WP) and the results are reported in Table 2. The crystallite size of the metal phosphide catalysts followed the order: MoP < WP < CoP < FeP < Ni_2P.

The water formation profiles of the calcined unsupported phosphate precursors are shown in Fig. 6. For $Ni_xP_yO_z$ sample, a shoulder at 468 ºC and two peaks at 515 and 578 ºC are observed. Taking into account the *in situ* diffractograms of this sample and reports from the literature [31-33], the shoulder and the peak at 515 ºC are likely due to the reduction of $Ni_2P_2O_7$ and $Ni_3(PO_4)_2$ to $Ni_{12}P_5$. The peak at high temperature is attributed to the reduction of $Ni_{12}P_5$ to Ni_2P.

The TPR profile of $Mo_xP_yO_z$ shows two peaks at 437 and 554 ºC. Bui et al. [27] also observed two peaks at around 375 and 520 ºC in the reduction profile of MoP/SiO_2 using phosphate precursor. The lower temperature peak was attributed to the reduction of MoO_3 to MoO_2, while the peak at high temperature was likely due to the reduction of molybdenum and phosphorous precursors to produce MoP. Similar TPR profile was observed for a calcined MoP/Al-SBA-15 sample [21]. In our work, the diffractogram of the calcined sample revealed the presence of $Mo(OH)_3PO_4$ phase. When the sample was heated, this phase decomposed, leading to the formation of MoO_3 and $MoOPO_4$ and amorphous content (Eqs. 4 and 5). No water evolution was detected in TPR profile because the phosphoric acid produced remains on the surface (Eq. 4). The peak at 437 ºC is likely due to the conversion of MoO_3 to $MoOPO_4$, while the formation of MoP occurs at 554 ºC by the reduction of $MoOPO_4$.

For $Co_xP_yO_z$, there is a hydrogen consumption between 500 and 530 ºC and a broad peak at 580 ºC . A broad twin-peak at high temperature has been reported on the reduction profile of phosphate precursor supported on SiO_2 [27], Al-SBA-15 [21], and HZSM-5 and Beta

zeolites [24]. These TPR profiles were attributed to the reduction of Co phosphate to metal and phosphine (PH_3) that reacts with the metal at high temperature producing CoP. In our work, the diffractogram of $Co_xP_yO_z$ sample did not show the formation of metallic cobalt. In fact, *in situ* XRD revealed the reduction of $Co(PO_3)_2$ phase to CoP_2 and CoP .

The TPR profile of FeP exhibits a shoulder and a peak with a maximum at 646 ºC. The reduction profile of FeP/SiO_2 exhibits a shoulder at 650 ºC and a peak at 750 ºC [27]. The authors proposed that iron phosphate was reduced to metallic Fe with the formation of PH_3, followed by the production of the phosphide. The diffractograms of unsupported $Fe_xP_yO_z$ sample of the present work showed that $FePO_4$ is reduced to $Fe_2P_2O_7$, which is converted to FeP at 645ºC. Therefore, the TPR profile of unsupported $Fe_xP_yO_z$ is in agreement with the XRD results.

The TPR of $W_xP_yO_z$ shows a shoulder at 624 ºC and a peak at 661 ºC. Clark et al. [41] reported a similar reduction profile for a silica supported WP sample, with a peak at 600 ºC. The authors proposed that tungsten precursor was reduced to W^0, which reacts with phosphine to produce WP. Unfortunatelly, the in situ XRD experiment was not carried out for this sample in our work and then, the attribution of the reduction peaks is not possible.

However, the diffractograms of all the unsupported metal phosphate precursors did not detected the formation of the metal phase. In fact, the *in situ* XRD experiments in our work shows that the phosphide phase is generally produced by the decomposition of the metal phosphate phase, followed by reduction to the metal phosphide, without the need to go through the formation of the metallic phase.

The values of CO chemisorption are presented on Table 2. All catalysts exhibit very low CO uptakes, which was not even detected for the Ni_2P. This is in agreement with previously reports [42,43].

The results may be correlated to the difference in the crystallite size of each reduced material. MoP and WP presented lower crystallite sizes, consequently more sites are exposed to adsorb CO. Similarly, Ni_2P has a very high crystallite diameter and, for this reason, no CO chemisorption could be detected during analyses. Finally, as CoP and FeP exhibited intermediate sizes of crystallite, intermediate chemisorption results, among the studied phosphides, were obtained for them.

3.2 HDO of phenol

Table 3 lists the phenol conversion, reaction rate and turnover frequencies calculated from XRD and CO chemisorption for HDO of phenol at 300 ºC over unsupported transition metal phosphide catalysts. The FeP phase exhibited the highest activity for deoxygenation that followed the order: FeP > MoP ≈ Ni_2P > WP ≈ CoP.

In our work, the intrinsic activity of each catalyst, represented by the turnover frequency, was calculated by two different methods, based on CO chemisorption and crystallite size calculated through XRD. The values are reported on Table 3.

The differences on the values of TOF may be attributed to a possible phosphorus deposition on the surface of the catalysts during its reduction or even due to aggregation of several crystallites to form each particle [40,44]. Therefore, there are blocked active sites that can not chemisorb probe molecules (CO or phenol), which inhibits the reaction rate. As the TOF calculated by crystallite diameter does not take into account these issues, it underestimates TOF values.

However, the crystallite size calculated by XRD for unsupported catalysts is not appropriated for estimating TOF because it does not consider that most of the crystallites are embedded in a solid with most of the surface in the interior grain boundaries. Therefore, the intrinsic activities of the catalysts, based on TOF calculated from CO chemisorption (most

reliable), were evaluated and followed the order: FeP > MoP > CoP ≈ WP. The TOF for Ni_2P can only be calculated from crystallite size diameter determined by XRD experiments and then, it was not evaluated due to the error associated to this measurement as previously mentioned.

The product distribution for HDO of phenol at 300 ºC and low phenol conversion over unsupported metal phosphide catalysts are reported on Table 4. Benzene was the main product observed for all catalysts, with formation of cyclohexene (ENE), cyclohexane (ANE), cyclohexanone (ONE) and C_5 – C_6 hydrocarbons (e.g., n-hexane, 2-methyl-butane). However, product distribution varied significantly depending on the metal phosphide phase. The Ni_2P catalyst exhibited the highest selectivity to benzene, whereas CoP, FeP and WP showed a significant formation of cyclohexene. FeP produced cyclohexene as well as cyclohexane, while a large amount of C_5 – C_6 hydrocarbons was formed over MoP. Furthermore, only minor amount of cyclohexanone was produced over all catalysts (less than 3.5 %).

The reaction mechanism for HDO of phenol over supported metal catalysts has been extensively studied in the literature [5-8,14,23-26,45]. One of the proposed mechanism is based on the tautomerization of phenol to a keto tautomer that can react by two different routes. This intermediate can be hydrogenated to cyclohexanone and then cyclohexanol, which may be dehydrated to cyclohexene. Then, cyclohexane is produced by hydrogenation of cyclohexene. This reaction route is favored over supports and metal oxides with enough acidity to promote dehydration. The other reaction pathway involves the hydrogenation of the carbonyl group of the keto tautomer intermediate, producing 2,4-cyclohexadienol, which is dehydrated to benzene.

Teles et al. [13,14] investigated the effect of the metal type on the reaction mechanism for HDO of phenol. They prepared two series of different metals (Pt, Pd, Rh,

Ru, Ni, Co) supported on SiO_2 and ZrO_2 and correlated the deoxygenation activity to the metal oxophilicity: Ru > Co > Ni > Rh > Pd > Pt. The authors also observed a significant formation of hydrogenolysis products (CH_4 and C_5-C_6 hydrocarbons) in addition to benzene over supported Ru catalyst. According to the literature [45], more oxophilic metals such as Ru strongly interact with the oxygen atom of the model molecule, reducing the energy barrier for the direct cleavage of the C-O bond of the aromatic ring (Direct deoxygenation – DDO). They proposed that the direct dehydroxylation of m-cresol over Ru leads to the formation of C_7H_7* unsaturated species. The hydrogenation of this intermediate produces toluene, while the cleavage of the C-C bonds is responsible for the production of CH_4 and C_5-C_6 hydrocarbons.

Recently, Gonçalves et al. [15] compared the performances of SiO_2 and ZrO_2 supported Ni^0 and Ni_2P catalysts for HDO of m-cresol. Supported Ni_2P catalysts exhibited higher deoxygenation activity than the supported metallic Ni catalysts. These results were attributed to a stronger adsorption of m-cresol over Ni_2P phase that favored the direct cleavage of C-O bond and the production of toluene in comparison to metallic Ni particles. De Souza et al. [25] reported similar results for HDO of phenol over NiP/SiO_2, NiP/TiO_2 and $NiP/CeZrO_2$ catalysts. The highest selectivity to benzene was likely due to the Ni_2P phase, suggesting that the phosphide phase promotes the direct deoxygenation pathway.

The direct deoxygenation of phenol route over transition metal phosphides was also demonstrated by theoretical calculations. He and Laursen [26] studied the deoxygenation over the 1st row transition metal phosphides (TiP, VP, CrP, Fe_2P, Co_2P, Ni_2P) using phenol as a model molecule and density functional theory. They reported that the metal phosphides exhibits an elevated surface chemical reactivity towards oxygen, which promotes the cleavage of C-O bond without the need for hydrogenation of phenol.

In our work, all metal transition phosphide catalysts exhibited high selectivity to benzene, indicating that the phosphide phases promoted the direct cleavage of C-O bond, regardless of the nature of the metal phosphide phase.

Table 4 also lists product distribution at low conversion for HDO of phenol in vapor phase at 300 ºC and atmospheric pressure over different catalysts. All unsupported phosphide catalysts exhibited higher selectivity to benzene than the different metal supported catalysts, except for Rh/Nb_2O_5. However, this catalyst contains noble metal, which is more expensive than the metal phosphide catalysts of our work.

MoP phase promoted also the formation of hydrogenolysis products, indicating that the intermediate species is strongly adsorbed and favored the C-C bond cleavage.

CoP, WP and FeP catalysts exhibited significant formation of cyclohexane and cyclohexene in comparison to Ni_2P. Rodríguez-Aguado et al. [23] also reported a high selectivity to cyclohexane and cyclohexene over FeP/SiO_2 for HDO of phenol in liquid phase, while Ni_2P/SiO_2 catalyst mainly produced cyclohexane and cyclohexanol. According to the authors, additional studies are required to understand the high selectivity to oxygen-free compounds of FeP phase.

According to the tautomerization mechanism proposed for HDO of phenol in gas phase [6,13], cyclohexane and cyclohexene could be formed over CoP, WP and FeP catalysts by two different reaction pathways. The first one involves the hydrogenation of benzene produced by the dehydration of the 2,4-cyclohexadienol. However, this reaction does not take place under the conditions used in our work. Therefore, cyclohexene and cyclohexane should be formed by the hydrogenation of the aromatic ring of the tautomer intermediate, producing cyclohexanone and cyclohexanol, which is dehydrated to cyclohexene and followed by its hydrogenation to cyclohexane. Scheme 1 shows the reaction pathway for the HDO of phenol over different transition metal phosphide phases.

There are only few works comparing the performance of several phosphides phases for the HDO of model molecules such as guaiacol and 2-methyltetrahydrofuran (2-MTHF). Unfortunatelly, no works about HDO of phenol using phosphide catalysts were found in the literature.

Zhao et al. [17] investigated the performance of different transition metal phosphides (Ni_2P, Co_2P, Fe_2P, MoP e WP) supported on SiO_2 for the HDO of guaiacol. Benzene and phenol were the main products formed, with minor amounts of methoxybenzene and C_3-C_5 hydrocarbons. The following order was observed for the selectivity to benzene, a product of total deoxygenation: $Ni_2P > Co_2P \approx MoP > Fe_2P \approx WP$. In fact, benzene was not detected over Fe_2P and WP phases, whereas phenol was the main product. In addition, hydrogenolysis products were fomed over MoP, as it was observed in our work.

Bui et al. [27] compared the activity of silica-supported transition metal phosphides for the HDO of 2-MTHF. For Ni_2P and CoP, the main products were pentane and butane, whereas pentenes and pentadienes were mainly produced over FeP, MoP and WP. The selectivity to HDO products followed the order: $MoP \approx WP > FeP > Ni_2P > CoP$.

The differences in the order of deoxygenation activity between our work from those of the literature are likely due to the different model molecules used (phenol, guaiacol, 2-MTHF) as well as to the different Co and Fe phosphide phases obtained.

These few works about HDO of different model molecules carefully investigated the reaction mechanisms and reported the trends for deoxygenation activity but they did not correlate the catalyst performance with the different phosphide phases.

For the metal phosphides, the metal atoms form triangular prisms or tetrakaidecahedral structure for metal-rich compositions [46]. The following crystal structures are reported for the different transition metal phosphides: MoP (WC_type hexagonal); Ni_2P (Fe_2P-type Orthohombic); WP, CoP, FeP (MnP-type Orthohombic). In our

work, the product distribution of metal phosphide catalysts seems to be affect by the type of crystal structure of transition metal phosphides. The direct deoxygenation is favored over WC_type hexagonal and Fe_2P-type Orthohombic, whereas MnP-type Orthohombic structure promotes the hydrogenation of the ring. The following order was observed for the direct deoxygenation selectivity: Ni_2P > MoP > CoP ≈ WP > FeP. This result is likely due to the phosphorus/metal ratio on the surface of each crystal structure. WC_type hexagonal and Fe_2P-type Orthohombic exhibit a higher phosphorus/metal ratio than MnP-type Orthohombic, which could lead to a stronger adsorption of the oxygen of the model molecule on the Ni cation. Gonçalves et al. [15] proposed that Ni sites on Ni_2P/SiO_2 catalyst surrounded by a higher number of phosphorus cations were responsible for the direct deoxygenation of m-cresol to toluene.

4. Conclusion

This work studied the synthesis of five unsupported transition metal phosphides (Nickel, Molybdenum, Cobalt, Iron and Tungsten) and their performance for HDO of phenol in gas phase.

In situ X-Ray diffraction and temperature programmed reduction investigated the evolution of different phases during reduction of metal phosphate phases. Initially, the metal phosphate precursor was decomposed to metal oxides (Molybdenum) or pyrophosphate (Nickel, Iron) phases, followed by the reduction and formation of the phosphide phases: Ni_2P, MoP, CoP/CoP_2, FeP and WP. The final activation temperature (650, 700 or 750 ºC) depended on the type of metal phosphide. No metallic phases were observed during the treatment under hydrogen

All catalysts exhibited high selectivity to direct deoxygenation products, which demonstrate that the metal phosphide phases promotes the direct cleavage of C-O bond. The

strong adsorption of the phenol on the metal phosphide particles decreases the energy barrier for the cleavage of the C-O bond. Meanwhile, the type of metal phosphide significantly affected product distribution. The highest selectivity to benzene was obtained for unsupported Ni_2P catalyst, while cyclohexene was mainly formed on CoP and WP. Cyclohexene as well as cyclohexane were produced over FeP, whereas C_5 – C_6 hydrocarbons were formed over MoP.

Therefore, transition metal phosphide catalysts have great potential for the deoxygenation of phenol to selectively produce aromatics.

Acknowledgments

This contribution is dedicated to the memory of Victor Teixeira da Silva. Priscilla M. de Souza and Carlos V. M. Inocêncio thanks Coordenação de Aperfeiçoamento de Pessoal de Nível Superior (CAPES – code finance 001) and Fundação de Amparo à Pesquisa do Estado do Rio de Janeiro (FAPERJ) for the scholarships. Fabio B. Noronha and Raimundo Crisostomo Rabelo-Neto also acknowledge the financial support of the Conselho Nacional de Desenvolvimento Científico e Tecnológico (CNPq - 303667/2018-4 and 301596/2020-4), Coordenação de Aperfeiçoamento de Pessoal de Nível Superior (CAPES-COFECUB program – 88881.142911/2017-01), Fundação de Amparo à Pesquisa do Estado do Rio de Janeiro (FAPERJ). The group also thanks the LNLS for the beamtime in XRD1 experimental line for the XRD analysis (Proposal 20180264).

References

[1] A.J. Ragauskas, C.K. Williams, B.H. Davison, G. Britovsek, J. Cairney, C.A. Eckert, W.J. Frederick Jr, J.P. Hallett, D.J. Leak, C.L. Liotta, J.R. Mielenz, R. Murphy, R. Templer, T. Tschaplinski, Science 311 (2006) 484-489.

[2] C. Xu, R.A.D. Arancon, J. Labidi, R. Luque, Chem. Soc. Rev. 43 (2014) 7485-7500.

[3] A.V. Bridgwater, Chem. Eng. J. 91 (2003) 87-102.

[4] D.M. Alonso, J.Q. Bond, J.A. Dumesic, Green Chem. 12 (2010) 1493-1513.

[5] P.M. De Souza, R.C. Rabelo-Neto, L.E.P. Borges, G. Jacobs, B.H. Davis, T. Sooknoi, D.E. Resasco, F.B. Noronha, ACS Catal. 5 (2015) 1318-1329.

[6] P.M. De Souza, R.C. Rabelo-Neto, L.E.P. Borges, G. Jacobs, B.H. Davis, D.E. Resasco, F.B. Noronha, ACS Catal. 7 (2017) 2058-2073.

[7] A.M. Barrios, C.A. Teles, P.M. De Souza, R.C. Rabelo-Neto, G. Jacobs, B.H. Davis, L.E.P. Borges, F.B. Noronha, Catal. Today 302 (2018) 115-124.

[8] C.A. Teles, P.M. De Souza, R.C. Rabelo-Neto, M.B. Griffin, C. Mukarakate, K.A. Orton, D.E. Resasco, F.B. Noronha, Appl. Catal. B 238 (2018) 38-50.

[9] S. Echeandia, B. Pawelec, V.L. Barrio, P.L. Arias, J.F. Cambra, C.V. Loricera, J.L.G. Fierro, Fuel 117 (2014) 1061-1073.

[10] D. Hong, S.J. Miller, P.K. Agrawal, C.W. Jones, Chem. Commun. 46 (2010) 1038-1040.

[11] C. Newman, X. Zhou, B. Goundie, I.T. Ghampson, R.A. Pollock, Z. Ross, M.C. Wheeler, R.W. Meulenberg, R.N. Austin, B.G. Frederick, Appl. Catal. A 477 (2014) 64-74.

[12] K.A. Resende, C.A. Teles, G. Jacobs, B.H. Davis, D.C. Cronauer, A.J. Kropf, C.L. Marshall, C.E. Hori, F.B. Noronha, Appl. Catal. B 232 (2018) 213-231.

[13] C.A. Teles, R.C. Rabelo-Neto, J.R. De Lima, L.V. Mattos, D.E. Resasco, F.B. Noronha, Catal. Lett. 146 (2016) 1848-1857.

[14] C.A. Teles, R.C. Rabelo-Neto, G. Jacobs, B.H. Davis, D.E. Resasco, F.B. Noronha, ChemCatChem 9 (2017) 2850-2863.

[15] V.O.O. Gonçalves, P.M. De Souza, T. Cabioc'h, V. Teixeira Da Silva, F.B. Noronha, F. Richard, Appl. Catal. B 219 (2017) 619-628.

[16] K. Li, R. Wang, J. Chen, Energ. Fuel 25 (2011) 854-863.

[17] H.Y. Zhao, D. Li, P. Bui, S.T. Oyama, Appl. Catal. A 391 (2011) 305-310.

[18] S.K. Wu, P.C. Lai, Y.C. Lin, H.P. Wan, H.T. Lee, Y.H. Chang, ACS Sustain. Chem. Eng. 1 (2013) 349-358.

[19] V.O.O. Gonçalves, P.M. De Souza, T. Cabioc'h, V. Teixeira Da Silva, F.B. Noronha, F. Richard, Catal. Commun. 119 (2019) 33-38.

[20] Z. Yu, Y. Wang, Z. Sun, X. Li, A. Wang, D.M. Camaioni, J.A. Lercher, Green Chem. 20 (2018) 609-619.

[21] A. Berenguer, T.M. Sankaranayaranan, G. Gómez, I. Moreno, J.M. Coronado, P. Pizarro, D.P. Serrano, Green Chem. 18 (2016) 1938-1951.

[22] V.M.L. Whiffen, K.J. Smith, Top. Catal. 55 (2012) 981-990.

[23] E. Rodríguez-Aguado, A. Infantes-Molina, D. Ballesteros-Plata, J.A. Cecilia, I. Barroso-Martín, E. Rodríguez-Castellón, Mol. Catal. 437 (2017) 130-139.

[24] A. Berenguer, S. Gutiérrez-Rubio, M. Linares, C. Ochoa-Hernández, I. Moreno, J.L. García-Fierro, J.M. Coronado, D.P. Serrano, P. Pizarro, Energy Technol. 7 (2019).

[25] P.M. De Souza, C.V.M. Inocêncio, V.I. Perez, R.C. Rabelo-Neto, V.O.O. Gonçalves, G. Jacobs, F. Richard, V. Teixeira Da Silva, F.B. Noronha, Catal. Today doi.org/10.1016/j.cattod.2019.08.028.

[26] Y. He, S. Laursen, Catal. Sci. Technol. 8 (2018) 5302-5314.

[27] P. Bui, J.A. Cecilia, S.T. Oyama, A. Takagaki, A. Infantes-Molina, H. Zhao, D. Li, E. Rodríguez-Castellón, A.J. López, J. Catal. 294 (2012) 184-198.

[28] W. Li, B. Dhandapani, S.T. Oyama, Chem. Lett. 27 (1998) 207-208.

[29] A.M.G. Carvalho, D.H.C. Araújo, H.F. Canova, C.B. Rodella, S.L. Cuffini, R.N. Costa, R.S. Nunes, J. Synchotron. Radiat. 23 (2016) 1501-1506.

[30] J. Wei, E. Iglesia, J. Catal. 224 (2004) 370-383.

[31] J.A. Rodriguez, J-Y. Kim, J.C. Hanson, S.J. Sawhill, M.E. Bussell, Journal of Physical Chemistry B, 107(26) (2003) 6276-6285.

[32] G. Berhault, P. Afanasiev, H. Loboué, C. Geantet, T. Cseri, C. Pichon, G-D Catherine, A.Lafond, Inorganic Chemistry 48(7) (2009), 2985-2992.

[33] X. Liu, L. Xu, B. Zhang, J. Solid State Chem. 212 (2014) 13-22.

[34] S.T. Oyama, X. Wang, Y.-K. Lee, K. Bando, F.G. Requejo, J. Catal. 210 (2002) 207-217.

[35] H. Okamoto, J. Phase Equilib. Diff. 31 (2010) 200-201.

[36] J.A. Cecilia, A. Infantes-Molina, E. Rodríguez-Castellón, A.J. López, S.T. Oyama, Appl. Catal. B 136-137 (2013) 140-149.

[37] S.E. Lister, V.J. Rixom, J.S.O. Evans, Chem. Mater. 22 (2010) 5279-5289.

[38] P.A. Clark, S.T. Oyama, J. Catal. 218 (2003) 78-87.

[39] A. Harilal, V.D.B.C Dasireddy, H.B. Friedrich, Catal. Lett. 146 (2016) 1169-1181.

[40] X. Wang, P. Clark, S.T. Oyama, J. Catal. 208 (2002) 321-331.

[41] P.A. Clark, W. Li, S.T. Oyama, J. Catal. 200 (2001) 140-147.

[42] S.T. Oyama, J. Catal. 216 (2003) 343-352.

[43] M. Peroni, G. Mancino, E. Baráth, O.Y. Gutiérrez, J.A. Lercher, Appl. Catal. B 180 (2016) 301-311.

[44] M. Behrens, R. Schlögl, "Characterization of Solid Materials and Heterogeneous Catalysts", 1st edition, v.2 Wiley-VCH, Weinheim, 2012, 609-653.

[45] Q. Tan, G. Wang, L. Nie, A. Dinse, C. Buda, J. Shabaker, D.E. Resasco, ACS Catal. 5 (2015) 6271-6283.

[46] S.T. Oyama, T. Gott, H. Zhao, Y.-K. Lee, Catal. Today 143 (2009) 94-107.

[47] K.A. Resende, F.B. Noronha, C.E. Hori, Renew. Energy 149 (2020) 198-207.

Figure captions

Figure 1 – *In situ* X-ray diffraction patterns obtained during reduction of $Ni_xP_yO_z$: (a) from room temperature to 650 ºC; (b) at selected temperatures.

Figure 2 – *In situ* X-ray diffraction patterns obtained during reduction of $Mo_xP_yO_z$: (a) from room temperature to 650 ºC; (b) at selected temperatures.

Figure 3 – *In situ* X-ray diffraction patterns obtained during reduction of $Co_xP_yO_z$: a) from room temperature to 650 ºC; (b) at selected temperatures.

Figure 4 – *In situ* X-ray diffraction patterns obtained during reduction of $Fe_xP_yO_z$: (a) from room temperature to 700 ºC; (b) at selected temperatures.

Figure 5 – *Ex situ* X-ray diffraction pattern obtained after reduction of $W_xP_yO_z$ at 750ºC.

Figure 6 – The water formation profiles of the calcined unsupported phosphate precursors at 1 ºC min^{-1} and pure H_2 flow.

Scheme 1- Reaction Routes for HDO of Phenol over Supported transition metal phosphide Catalysts

(a)

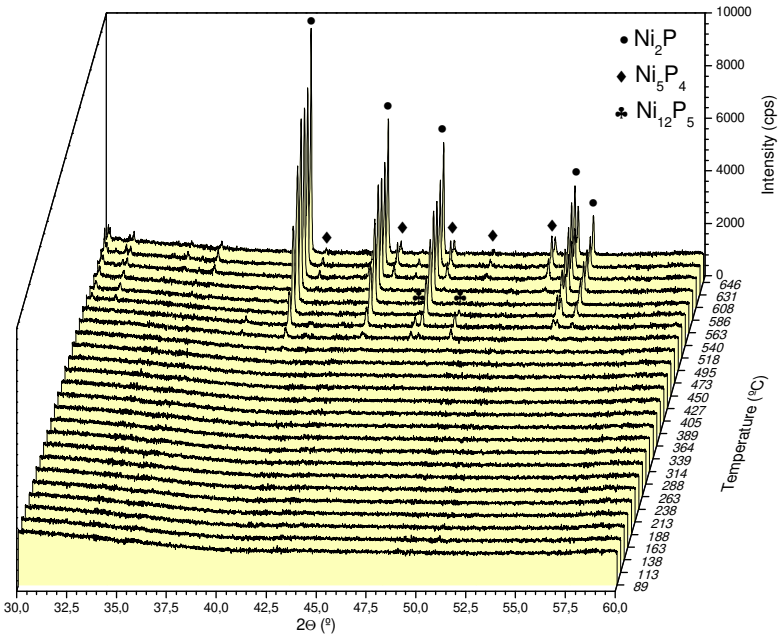

(b)

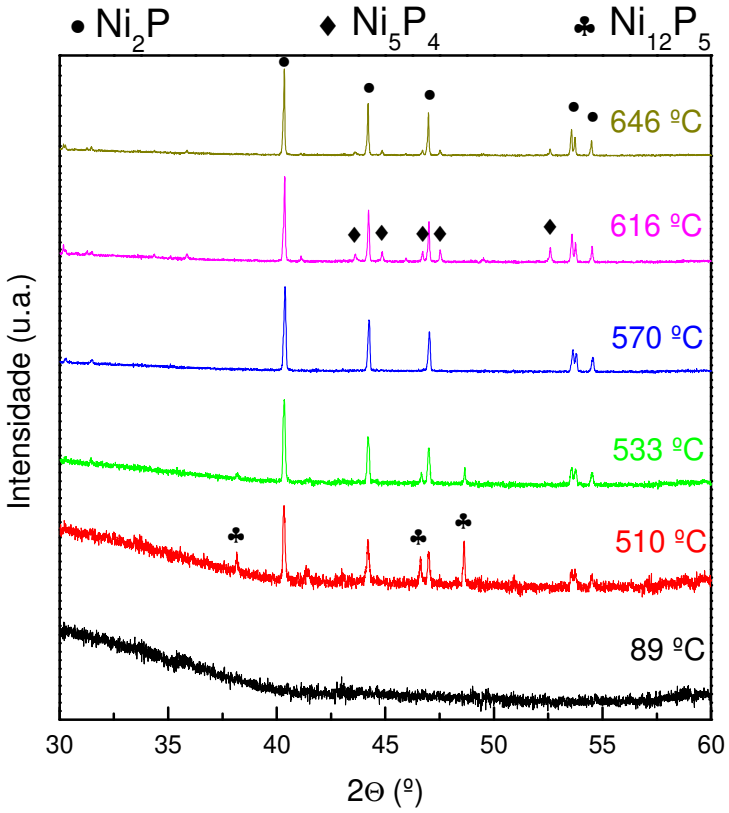

Figure 1 – *In situ* X-ray diffraction patterns obtained during reduction of $Ni_xP_yO_z$: (a) from room temperature to 650 ºC; (b) at selected temperatures.

(a)

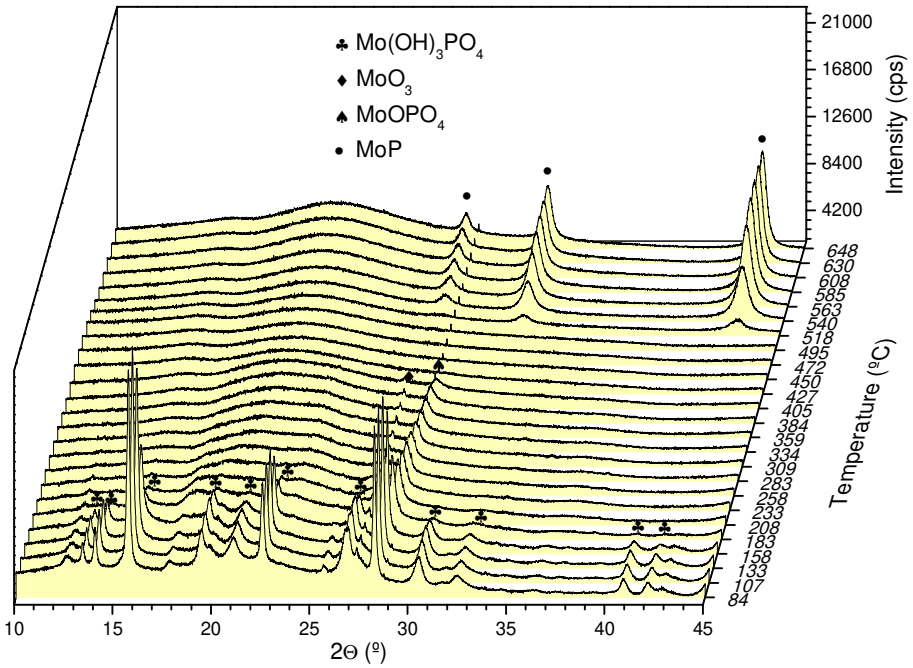

(b)

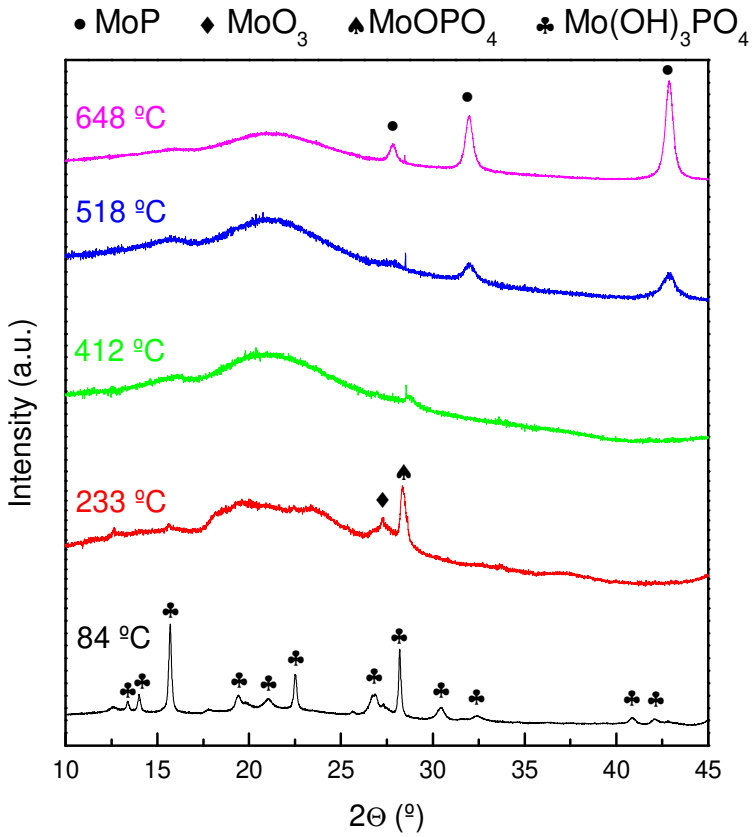

Figure 2 – *In situ* X-ray diffraction patterns obtained during reduction of $Mo_xP_yO_z$: (a) from room temperature to 650 ºC; (b) at selected temperatures.

(a)

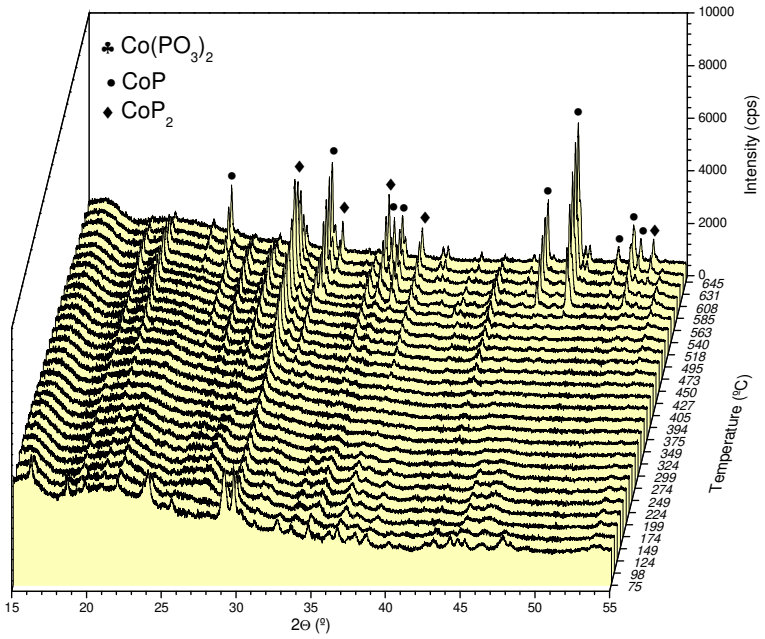

(b)

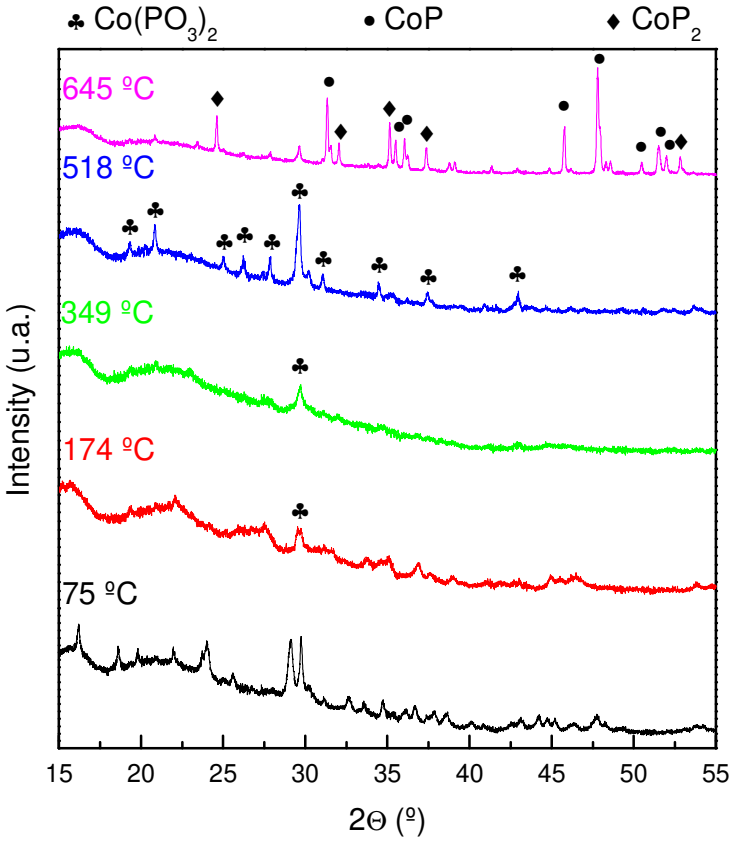

Figure 3 – *In situ* X-ray diffraction patterns obtained during reduction of $Co_xP_yO_z$: a) from room temperature to 650 ºC; (b) at selected temperatures.

(a)

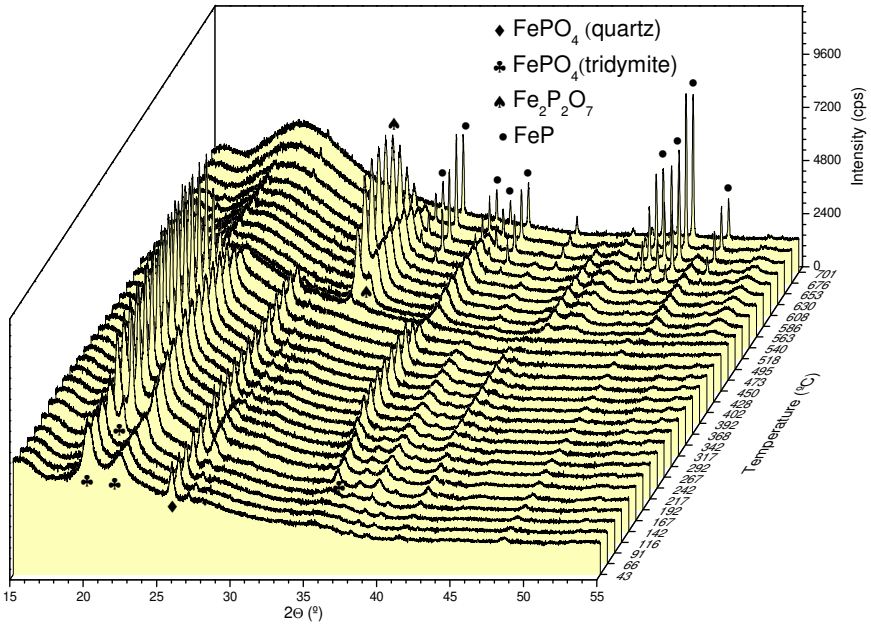

(b)

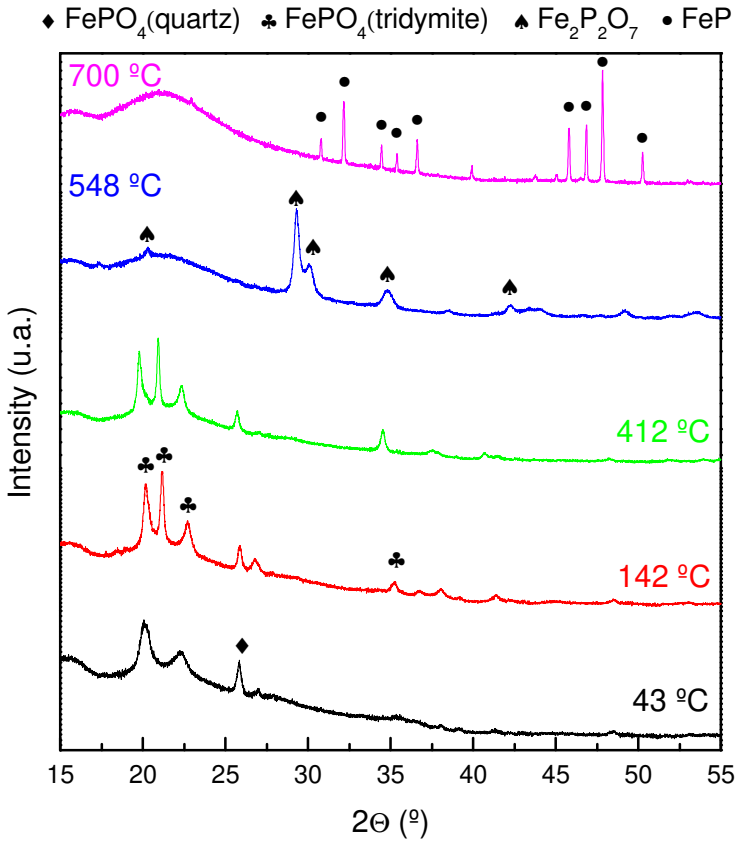

Figure 4 – *In situ* X-ray diffraction patterns obtained during reduction of $Fe_xP_yO_z$: (a) from room temperature to 700 ºC; (b) at selected temperatures.

.

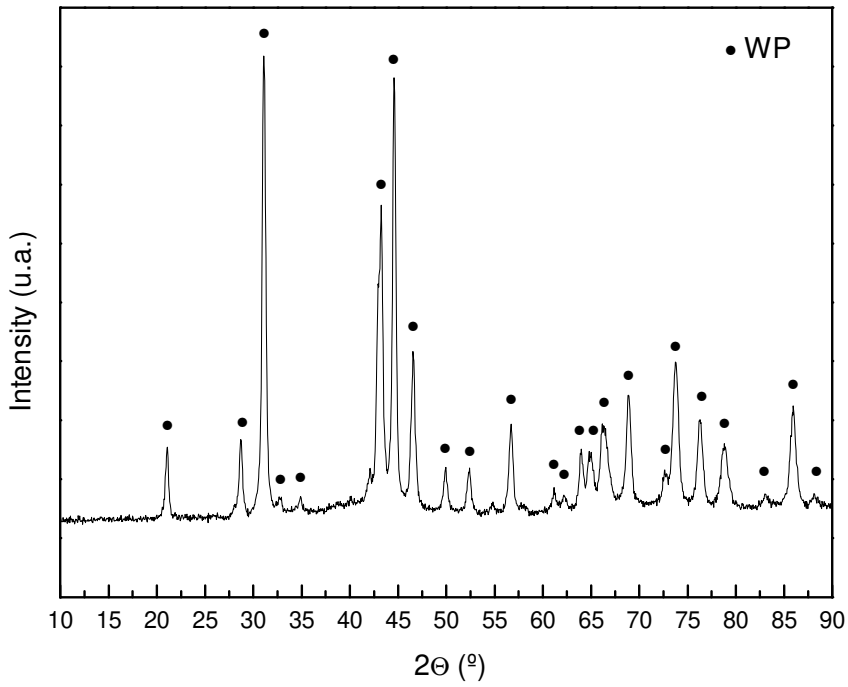

Figure 5 – *Ex situ* X-ray diffraction pattern obtained after reduction of $W_xP_yO_z$ at 750ºC.

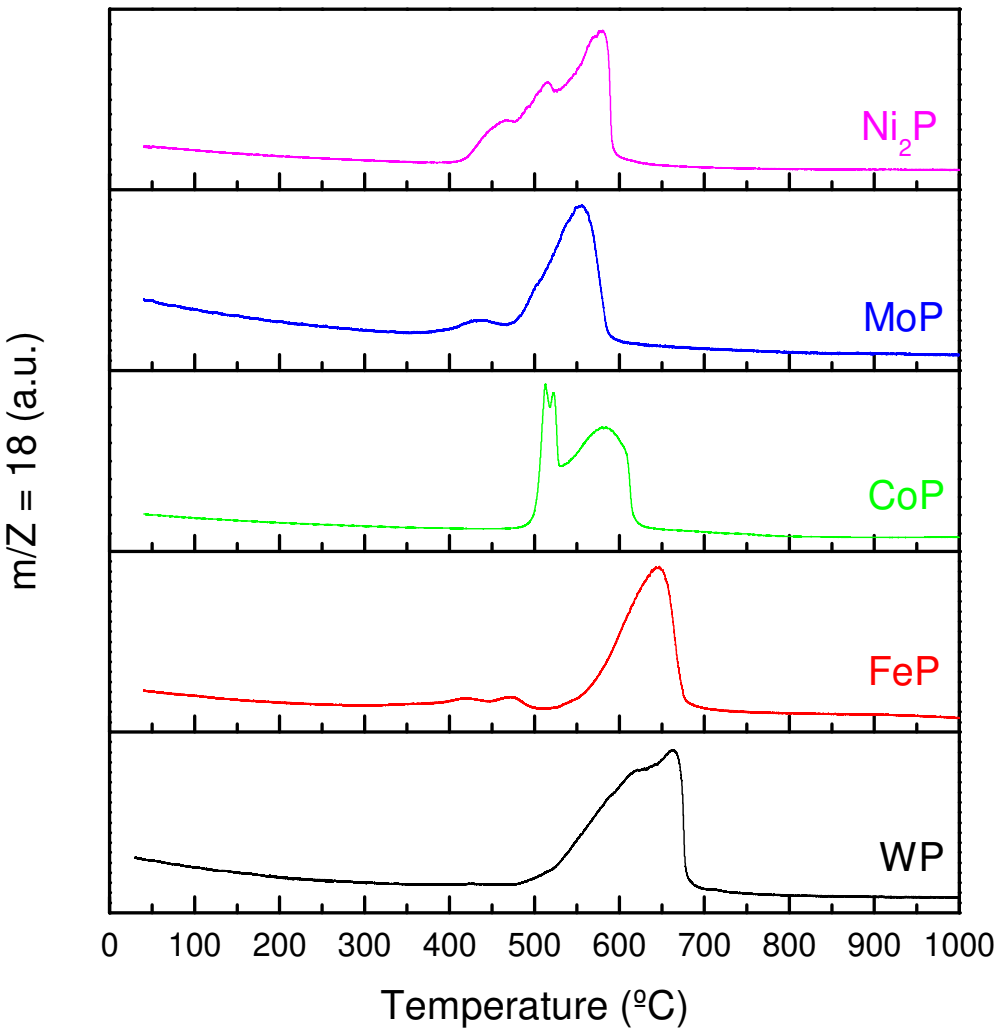

Figure 6 – The water formation profiles of the calcined unsupported phosphate precursors at 1 ºC min^{-1} and pure H_2 flow.

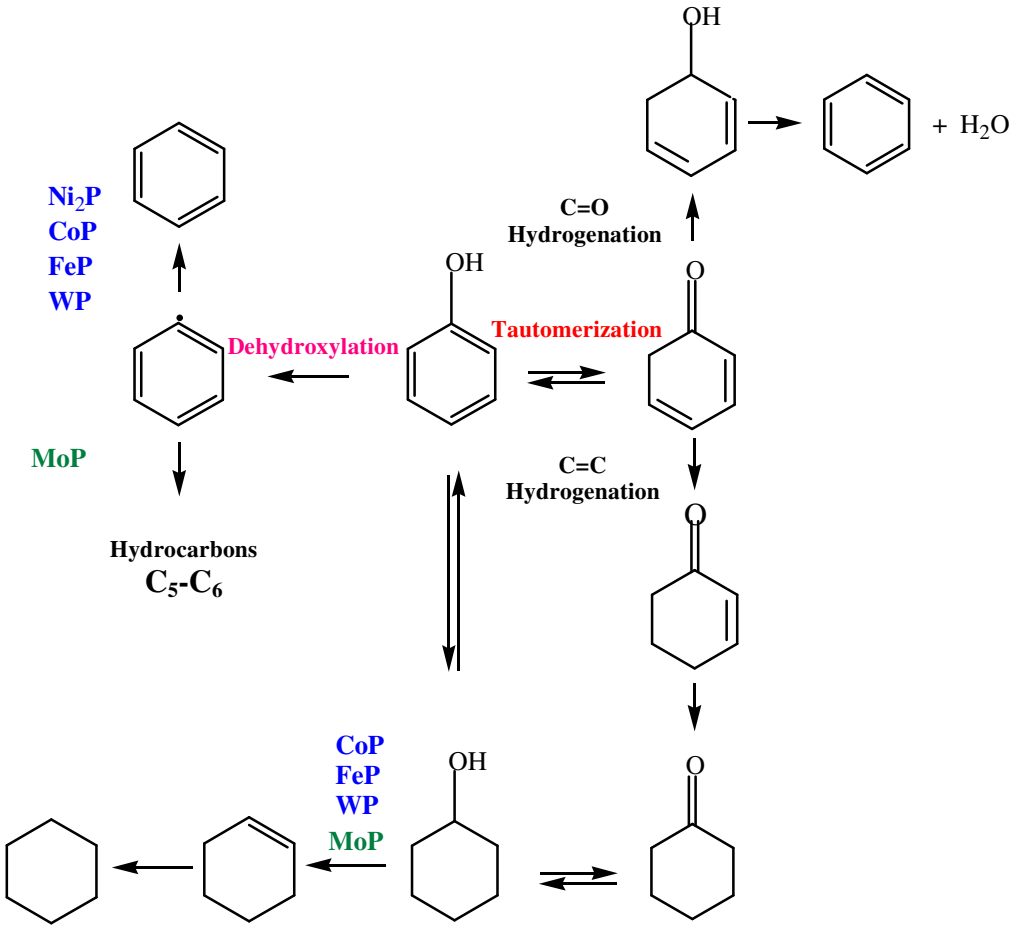

Scheme 1- Reaction Routes for HDO of Phenol over Supported transition metal phosphide Catalysts

Table 1 – Intermediate (T_1) and final (T_2) activation temperatures employed in the syntheses of the phosphides.

Phosphide	**T_1 (°C)**	**T_2 (°C)**
Ni_2P	350	650
CoP	400	650
FeP	300	700
MoP	300	650
WP	400	750

Table 2 – CO uptake, and crystallite size calculated from CO chemisorption (d_{CO}) and XRD (d_{XRD}) for metal phosphide catalysts.

Catalyst	**d_{XRD} (nm)**	**n_{CO} (µmol g^{-1})**	**d_{CO} (nm)**
Ni_2P	108	ND	ND
CoP	45	12	927
FeP	77	7	1645
MoP	16	16	492
WP	27	22	212

ND: CO adsorption not detected

Table 3 – Reaction rate and turnover frequencies calculated through XRD and CO chemisorption for HDO of phenol at 300 ºC and low phenol conversion over unsupported metal phosphide catalysts.

Catalyst	Catalyst weight (mg)	Conversion (%)	r (μmol min^{-1} g^{-1})	r_{HDO} (μmol min^{-1} g^{-1})	TOF_{CO} (min^{-1})	TOF_{XRD} (min^{-1})
Ni_2P	101.4	4.5	9.5	9.2	-	0.08
CoP	208.7	5.1	5.3	5.1	0.44	0.02
FeP	151.0	9.4	13.6	13.3	1.94	0.09
MoP	140.4	7.1	10.8	10.8	0.67	0.02
WP	176.8	5.2	6.2	6.2	0.28	0.04

Table 4 - Product distribution for HDO of phenol in gas phase at 300 ºC, 1 atm and low conversion over unsupported metal phosphide catalysts of this work and with different catalysts from the literature. Benz – Benzene; ONE – Cyclohexanone; OL – Cyclohexanol; ANE – Cyclohexane; ANE – Cyclohexene.

Catalysts	Conversion (%)	Product distribution (%)								
		Benz	ONE	OL	C_5-C_6	CH_4	C_{12}	ANE	ENE	Refer.
Ni_2P	4.5	94.6	2.8	--	--	--	--	1.4	1.2	Present work
CoP	5.1	84.2	3.1	--	--	--	--	1.0	11.7	Present work
WP	5.2	82.7	--	--	--	--	--	1.6	15.7	Present work
FeP	9.4	75.3	1.6	0.4	--	--	--	12.0	10.7	Present work
MoP	7.1	57.5	--	--	29.6	--	--	6.2	6.6	Present work
Pt/ZrO_2	9.3	27.4	56.6	12.8	1.8	--	1.4			14
Pd/ZrO_2	8.2	43.2	52.6	1.7	0.1	--	2.4			14
Rh/ZrO_2	8.8	63.4	22.0	--	9.1	5.2	0.3			14
Ru/ZrO_2	8.3	49.7	5.6	0.8	14.9	27.3	9.6			14
Ni/ZrO_2	11.4	26.7	37.7	10.9	0.8	15.4	2.8			14
Pt/SiO_2	13.2	0.8	88.0	11.0	--	--	0.2			13
Pd/SiO_2	17.1	3.3	93.7	3.0	--	--	--			13
Rh/SiO_2	9.4	3.1	85.3	4.2	7.2	--	0.2			13
Ru/SiO_2	12.4	5.8	19.4	3.4	8.7	62.3	0.4			13
Ni/SiO_2	14.7	4.8	63.6	20.0	1.2	7.2	1.2			13
Pd/Nb_2O_5	5.6	72.4	25.3	--	--	--	--	--	2.3	47
Rh/Nb_2O_5	10.3	92.6	3.1	--	--	--	--	--	4.3	47
Ni/Nb_2O_5	8.3	60.2	30.2	--	--	--	--	--	9.6	47

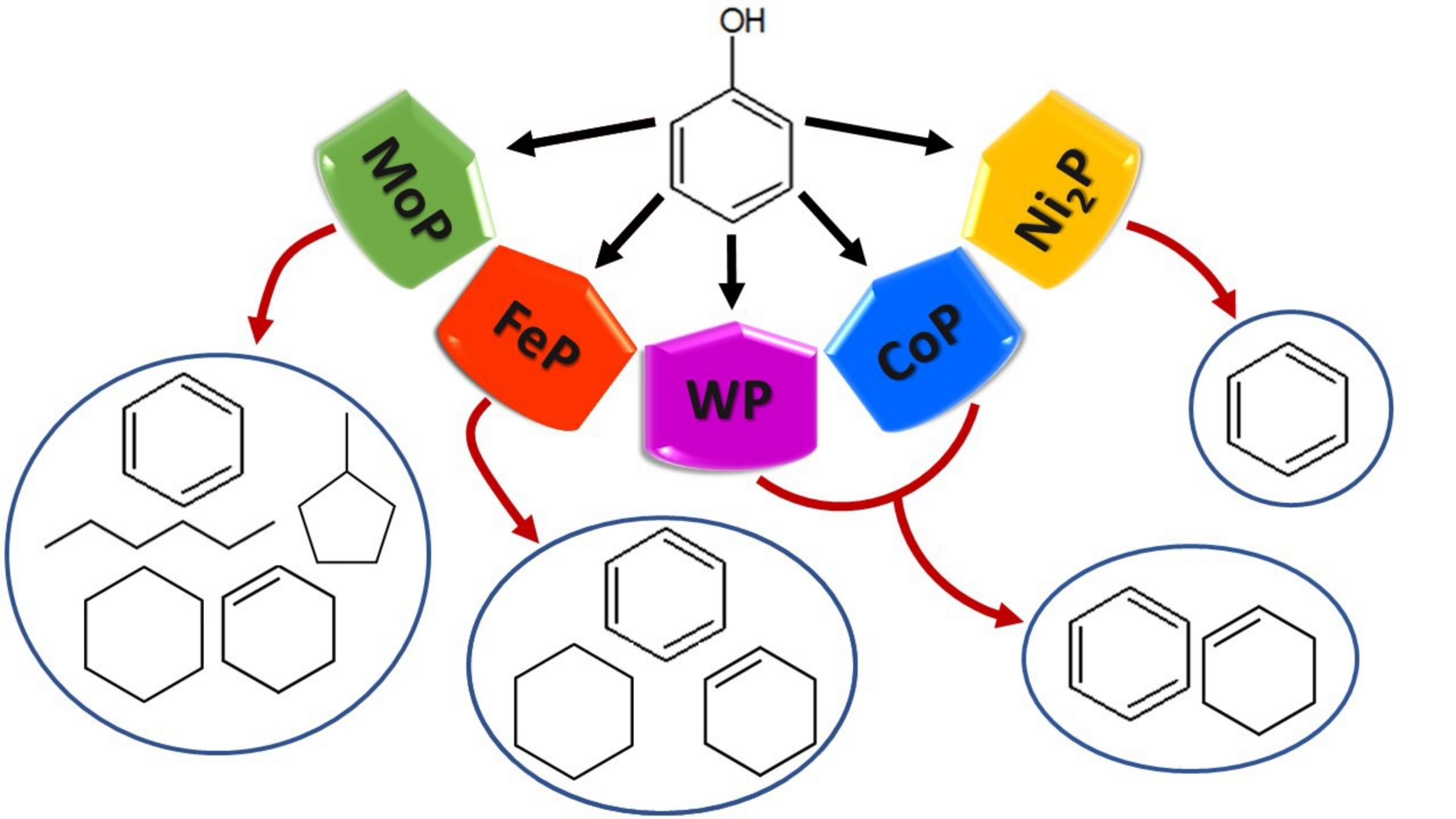
OH
MoP
FeP
WP
CoP
Ni2P